J. Non-Newtonian Fluid Mech. 156 (2009) 112–120

Contents lists available at ScienceDirect

Journal of Non-Newtonian Fluid Mechanics

journal homepage: www.elsevier.com/locate/jnnfm

Stress communication and filtering of viscoelastic layers in oscillatory shear

Brandon Lindley[a,*,1], Eddie Lee Howell[b], Breannan D. Smith[b], Gregory J. Rubinstein[b], M. Gregory Forest[a], Sorin M. Mitran[a], David B. Hill[c], Richard Superfine[d]

[a] Center for Interdisciplinary Applied Mathematics, Department of Mathematics, University of North Carolina, Chapel Hill 27599-3250, United States
[b] The Virtual Lung Project and Department of Mathematics, University of North Carolina, Chapel Hill 27599-3250, United States
[c] Cystic Fibrosis Center, University of North Carolina, Chapel Hill 27599-7248, United States
[d] Department of Physics and Astronomy, University of North Carolina, Chapel Hill 27599-3250, United States

ARTICLE INFO

Article history:
Received 10 March 2008
Received in revised form 14 July 2008
Accepted 28 July 2008

Keywords:
Stress propagation
Large amplitude oscillatory shear
Shear waves
Upper convected Maxwell model
Biological layers

ABSTRACT

We revisit a classical topic: response functions of viscoelastic layers in large amplitude oscillatory shear. Motivated by questions concerning protective biological layers, we focus on boundary stresses in a parallel plate geometry with imposed oscillatory strain or stress. These features are gleaned from resolution and analysis of coupled standing waves of deformation and stress. We identify a robust non-monotone variation in boundary stress signals with respect to all experimental controls: viscoelastic moduli of the layer, layer thickness, and driving frequency. This structure of peaks and valleys in boundary values of shear and normal stress indicates redundant mechanisms for stress communication (by tuning to the peaks) and stress filtering (by tuning to the valleys). In this paper, we first restrict to a single-mode nonlinear Maxwell model for the viscoelastic layer, where analysis renders a transparent explanation of the phenomena. We then consider a Giesekus constitutive model of the layer, where analysis is supplanted by numerical simulations of coupled non-linear partial differential equations. Parametric studies of wall stress values from standing waves confirm persistence of the Maxwell model phenomena. The analysis and simulations rely on and extend our recent studies of shear waves in a micro parallel plate rheometer [S.M. Mitran, M.G. Forest, L. Yao, B. Lindley, D. Hill, Extenstions of the Ferry shear wave model for active linear and nonlinear microrheology, J. Non-Newtonian Fluid Mech. 154 (2008) 120–135; D.B. Hill, B. Lindley, M.G. Forest, S.M. Mitran, R. Superfine, Experimental and modeling protocols from a micro-parallel plate rheometer, UNC Preprint, 2008].

1. Introduction

The behavior of viscoelastic layers in large amplitude oscillatory shear (LAOS) has been studied in depth in the rheology literature. The methods of inquiry are varied, ranging from presumed homogeneous deformations where the problem analytically reduces to a dynamical system of ordinary differential equations [7,12,11], to presumed one-dimensional heterogeneous deformations where the models are coupled with systems of partial differential equations [4], to two-dimensional heterogeneity and the need for demanding numerical solver technology [6].

In LAOS, the rheological focus is typically on departures from linear responses and good metrics for capturing the onset and degrees of non-linearity in the system. We refer to [7] and [9,10] for a scholarly treatment of the phenomenological signature of non-linearity. A key diagnostic for divergence from linear behavior is the Lissajous figure of shear stress (τ_{xy}) versus shear rate ($\dot{\gamma}$) [17]. In the linear regime, the ($\dot{\gamma}(t)$, $\tau_{xy}(t)$) Lissajous figures are characterized by thin ellipses which distort in various ways in the non-linear regime [7].

The phenomenon of interest for this paper is motivated by a biological query. There are countless examples in biology where a viscoelastic layer plays a vital mechanistic function; mucus appears to be one of Nature's favorite materials. The work of Hosoi and co-workers has explored snail mucus and locomotion principles [8]. Our focus arises from lung biology, where mucus layers line pulmonary pathways and serve as the medium between air from the external environment and the cilia–epithelium complex. The typical transport mechanism explored is mucociliary clearance, in which pathogens and environmental particulates are trapped by mucus while coordinated cilia propel the mucus layer toward the larynx. However, Tarran et al. [13] have documented the role of oscillatory stress in regulating biochemical release rates of epithelial cells. This discovery raises fundamental questions about the stress signals arriving either at cilia tips or directly to epithelial

* Corresponding author.
E-mail address: lindleyb@math.sc.edu (B. Lindley).
[1] Now currently a postdoctoral researcher at the University of South Carolina, Columbia, SC, 29208, United States.

0377-0257/$ – see front matter © 2008 Elsevier B.V. All rights reserved.
doi:10.1016/j.jnnfm.2008.07.013

cells from a sheared mucus layer. Air-drag stresses from either tidal breathing or cough are communicated through the mucus layer to the opposing interface, whereas cilia-induced strain generates stress at the same interface. This context leads us to explore one driven interface of a viscoelastic layer, either by frequency-dependent strain or stress, and then to monitor the stress or strain at both interfaces. We are intrigued by the notion that the dynamic moduli and thickness of the mucus layer are part of the feedback loop in the lung by virtue of the stresses and strains they transmit to cells. The mechanism explored by Tarran et al. [13] could simply imply that stronger amplitudes of applied strain or stress are employed to trigger biochemical releases. However, a more intriguing hypothesis will emerge from the results presented here. Namely, at the same applied strain or stress level, such as from tidal breathing or coordinate ciliary beating, a tuning of wall stresses is achievable by changes in either viscoelastic properties or thickness of the mucus layer or the frequency of driving. With these motivations, we move now to an idealized model and geometry to explore these phenomena.

For this paper, we impose oscillatory strain and explore interfacial stresses generated from standing waves of stress and deformation in a viscoelastic layer; later we return to the relationship between imposed stress versus strain. This formulation matches the experimental configuration of finite-depth "Ferry-Stokes" viscoelastic shear waves, for which we have recently built experimental [5] and modeling [4] tools. Thus, we have ready software and analytical understanding of the coupled flow and stress waves in an oscillatory strain-driven viscoelastic layer. We first analyze boundary values of shear stress, followed by the generation of normal stresses through non-linear material properties. We emphasize that we are interested in the space of solutions of this time-dependent boundary value problem, and their variations with respect to all control parameters in the problem: layer thickness, frequency of driving, and dynamic moduli of the material at the driving frequency. We focus on the upper convected non-linearity as the common feature of all non-linear continuum mechanical laws [14,15]; the results remain robust in the presence of other non-linearities, such as the Giesekus model, where these phenomena were first discovered through numerical studies.

The remainder of the paper is organized as follows: we first recall the formulation of the model, and basic mathematical properties of the time-dependent, one-space dimensional viscoelastic solutions relevant to oscillatory strain boundary conditions from [4]. Next, we proceed to explore stress communication. Because of non-linearity, the analogous results with imposed oscillatory stress do not follow from the strain results: a single frequency input strain yields full harmonic stress response, and vice versa. However, in the "homeostatic response", where one focuses on the frequency-locked response to the periodic strain driving condition, we can work out the precise relationship between oscillatory strain-controlled and stress-controlled experiments (Section 6) for the upper convected Maxwell model, another argument for special attention to this simplest of all non-linear differential constitutive laws.

We organize boundary stress signals in terms of "transfer functions" which convey specific information about the response of the viscoelastic layer. The transfer functions for this paper are the extreme maximum normal and shear stress signals arriving at either plate in oscillatory strain experiments, maximized or minimized over the period of the frequency-locked response of the layer. Shear stresses oscillate with mean zero, so there is no need to track their minima. First normal stress differences of the UCM model are non-negative, so their extreme convey the bounds on normal stress generation. These transfer functions are functions of material and experimental parameters and our focus becomes the behavior with respect to each argument. The first illustration is the behavior of the extreme boundary shear and normal stress signals for a series of experiments where the layer height is varied; we illustrate with three "model fluids" ranging from a highly elastic to a viscoelastic to a simple viscous fluid. We show that the maximum normal and shear wall stresses exhibit strong peaks at discrete depths, with a significant drop between the peaks; this structure disappears in the viscous fluid limit. We then extend the results to all other parameters. Finally, to show robustness of the behavior, we shift to the Giesekus model. We generate parameter sweeps of the stress transfer functions, which now require numerical simulations of the governing system of non-linear partial differential equations at each fixed parameter set. The oscillatory structure in these boundary stress signals persists; as noted earlier, we discovered this parametric dependence of wall stresses from the Giesekus code, so the issue of persistence was never in doubt.

2. Mathematical model

We recall the formulation developed in [4,5], which is a generalization of the Ferry shear wave model [1–3] to finite depth layers and non-linear constitutive laws. We summarize the key elements from these references in order to describe the present focus on boundary stress signals in oscillatory strain experiments. The equations of motion for an incompressible fluid are[2]

$$\rho\left(\frac{\partial\vec{v}}{\partial t}+(\vec{v}\cdot\nabla)\vec{v}\right)=\nabla\cdot\mathbf{T} \tag{1}$$

$$\nabla\cdot\vec{v}=0, \tag{2}$$

where $\boldsymbol{T}$ is the total stress tensor, $\vec{v}$ is the fluid velocity, and ρ is the fluid density. The total stress tensor is decomposed as $\boldsymbol{T}=-pI+\boldsymbol{\tau}$ and then the constitutive properties of the viscoelastic material are prescribed for $\boldsymbol{\tau}$, the "extra stress tensor." The term p, often called "pressure," is the isotropic contribution to the total stress tensor. We refer the reader to the recent discussion by Dealy [16] on pressure measurements and inferences in rheological experiments.

We restrict attention to the simplest non-linear constitutive law, the Upper Convective Maxwell (UCM) model, which possesses the convective non-linearity that is common to all non-linear constitutive models. In this model, the viscoelastic properties are coarse-grained into a single elastic relaxation time (λ_0) and a single zero-shear-rate viscosity (η_0):

$$\lambda_0\overset{\nabla}{\boldsymbol{\tau}}+\boldsymbol{\tau}=2\eta_0\boldsymbol{D}, \tag{3}$$

where $\boldsymbol{D}$ is the rate-of-strain tensor, $\boldsymbol{D}=1/2(\nabla\vec{v}+\nabla\vec{v}^T)$, and the upper convected derivative is defined as

$$\overset{\nabla}{\boldsymbol{\tau}}=\frac{\partial t}{\partial t}+(\vec{v}\cdot\nabla)\boldsymbol{\tau}-\nabla\vec{v}^T\cdot\boldsymbol{\tau}-\boldsymbol{\tau}\cdot\nabla\vec{v}. \tag{4}$$

We assume one-dimensional shear flow in the x direction between the parallel plates and that vorticity is negligible, so that $v_y=v_z=0$. The two parallel plates remain at heights $y=0$ and $y=H$, with strain controls on the lower plate given by the displacement amplitude A and oscillation frequency ω. This boundary control can be stated in terms of boundary conditions on the primary velocity v_x at $y=0$,

$$v_x(0,t)\equiv V_0\sin\ (\omega t),\quad \text{(BC1)} \tag{5}$$

[2] Throughout this paper, arrows will indicate column vectors, while bold symbols indicate tensors.

where $V_0 = A\omega$, while the top plate is held stationary for the purposes of this paper, which corresponds to

$$v_x(H, t) \equiv 0. \quad \text{(BC2)} \tag{6}$$

The self-consistent reduction of stress yields $\tau_{xz} = \tau_{yz} = \tau_{zz} = 0$. The full model (1–4) reduces to the following closed system of partial differential equations for the remaining unknowns (v_x, p, τ_{xx}, τ_{yy}), which are functions of the gap height (y) and time:

$$\rho \frac{\partial v_x}{\partial t} = \frac{\partial \tau_{xy}}{\partial y} \tag{7}$$

$$\frac{\partial p}{\partial y} = \frac{\partial \tau_{yy}}{\partial y} \tag{8}$$

$$\lambda_0 \frac{\partial \tau_{xx}}{\partial t} - 2\lambda_0 \frac{\partial v_x}{\partial y}\tau_{xy} + \tau_{xx} = 0 \tag{9}$$

$$\lambda_0 \frac{\partial \tau_{xy}}{\partial t} - \lambda_0 \frac{\partial v_x}{\partial y}\tau_{yy} + \tau_{xy} = \eta_0 \frac{\partial v_x}{\partial y} \tag{10}$$

$$\lambda_0 \frac{\partial \tau_{yy}}{\partial t} + \tau_{yy} = 0. \tag{11}$$

We are only concerned with "homeostatic" responses for this study, in particular the frequency-locked response of the fluid layer to the boundary control. Thus we suppress the effects of transients and initial conditions on velocity, "pressure" and stress. From (11), τ_{yy} decays exponentially to zero, and from (8) any gradient of p, will likewise converge rapidly to zero. In [4], a complete solution of this problem is derived resting on the observation that v_x and τ_{xy} decouple into a linear hyperbolic system once τ_{yy} is negligible, and then the remnant of non-linearity from the upper convective derivative reduces to the solution of (8) with known functions for the velocity and shear stress. The 2×2 system (7, 9, satisfying BC1 and BC2) is solved, in the $H = \infty$ limit by Ferry et al. [1–3], and generalized to any finite H by the authors [4]:

$$v_x(y, t) = Im\left(V_0\ e^{i\omega t}\frac{\sinh(\delta(H-y))}{\sinh(\delta H)}\right) \tag{12}$$

$$\tau_{xy} = Im\left(-V_0\eta^*\delta\ e^{i\omega t}\frac{\cosh(\delta(H-y))}{\sinh(\delta H)}\right). \tag{13}$$

Here we have introduced the complex viscosity, $\eta^* = \eta' = i\eta''$, which for a single-mode Maxwell fluid is

$$\eta' = \frac{\eta_0}{1 + (\omega\lambda_0)^2} \tag{14}$$

$$\eta'' = \frac{\eta_0\omega\lambda_0}{1 + (\omega\lambda_0)^2}. \tag{15}$$

The key complex parameter in the response functions for v_x and τ_{xy} is

$$\delta = \alpha + i\beta, \tag{16}$$

the same notation and parameter identified by Ferry in the semi-infinite layer limit, which is given for the single mode Maxwell model by:

$$\alpha = \sqrt{\frac{\rho\omega}{2\eta_0}\left(\sqrt{1 + \omega^2\lambda_0^2} - \omega\lambda_0\right)} \tag{17}$$

$$\beta = \sqrt{\frac{\rho\omega}{2\eta_0}\left(\sqrt{1 + \omega^2\lambda_0^2} + \omega\lambda_0\right)}. \tag{18}$$

This solution, though written here for the UCM model, is a special case of the solution for a general linear viscoelastic fluid [4,1]. The real parameters α and β correspond physically to the attenuation length and wavelength described by Ferry in the semi-infinite domain problem. In the finite depth layer, our formulas resolve counter-propagating waves and thus the physical significance of α and β is not transparent in a snapshot; instead we have developed inverse characterization protocols based on microbead tracking and single particle paths [5].

We proceed now to the focus of this discussion, namely stress boundary signals. With the exact expressions for v_x and τ_{xy}, the evolution of τ_{xx} is now explicitly given by a quadrature solution of (8), where initially τ_{xx} is assumed to be zero:

$$\tau_{xx}(y, t) = 2\int_0^t e^{(t'-t)/\lambda_0}\frac{\partial v_x}{\partial y}(y, t')\tau_{xy}(y, t')\ dt'. \tag{19}$$

The convolution integral cannot be carried out explicitly (at least not under the weight of our pen thus far), but can be numerically evaluated. The transfer functions of interest are then given for the UCM model by evaluation of formulas (12), (13) and (19) at $y = 0$ or $y = H$. Note that since $\tau_{yy} = 0$ in the UCM model after transients have passed, the first normal stress difference $N_1 = \tau_{xx} - \tau_{yy}$ and τ_{xx} are used interchangeably until we get to the Giesekus model simulations.

3. Experimental and biological relevance and limitations

It is worth noting some of the inherent limitations of this model for literal biological applications. First, we have mapped the cylindrical pathway to a parallel plate geometry, which suppresses curvature effects. We have also ignored the asymmetry of the coordinated cilia oscillatory pattern, thus removing the translational component of the layer response. Thus our models are faithful to the micro parallel plate rheometer [5], and the extension of these results to an air pathway remains for the future. This simplified geometry allows us to identify the fundamental mechanism of boundary stress variations with respect to all experimental controls. Within this model geometry, there remain potential sources of error, starting with the effects of the sidewalls, which Ferry and coworkers analyzed in their original papers. In our device, the aspect ratio of the gap height to the transverse dimensions is extremely small (between 1:20 and 1:100) relative to Ferry's apparatus, where the aspect ratio is order 1. Therefore, the transverse component of waves in our device (due to slightly non-parallel plates) travel far greater distances where the attenuation properties of the medium dominate. The boundary conditions in the lateral directions, where there is a meniscus, are continuity of stress, which will further suppress back-propagation relative to the Ferry apparatus.

At this point, we are encouraged by the comparison of the model predictions with experimental data [5]. The biological relevance of the predictions of this paper to *in vivo* pulmonary stress signaling remains a future challenge.

4. Stress selection criteria

The primary focus of most studies of large amplitude oscillatory shear (LAOS) is on the dynamic (time-dependent) responses in a given experiment. The dynamic response functions sometimes presume homogeneous deformations [7] while other studies explore heterogeneity [6]. Our study admits one-dimensional heterogeneity, but we are interested in stress information arriving at layer boundaries. For a given realization of the experiment, we extract the extreme boundary shear and normal stress signals arriving at either the driven interface or the opposing stationary interface. The wall shear stress oscillates with mean zero and the maximum and minimum values have the same magnitude, so only the maximum

of shear stress is reported. The normal stress τ_{xx} is non-negative. Extreme values of both shear and normal stress are reported. These "transfer functions" are denoted: $\max_t \tau_{xy}(0,t)$, $\max_t \tau_{xy}(H,t)$, $\max_t \tau_{xx}(0,t)$, $\min_t \tau_{xx}(0,t)$, $\max_t \tau_{xy}(H,t)$, and $\min_t \tau_{xx}(H,t)$. To begin the discussion we consider $\max_t \tau_{xy}(0,t)$. Later, after we identify salient features of these transfer functions, we return to the more traditional Lissajous figures of the time-dependent stress and shear rate. At that point, we show wall stress fluctuations with parameters translate to Lissajous figure fluctuations.

4.1. Analysis of interfacial stress signals

Consider the following "layer" transfer function: the maximum shear stress of the frequency-locked response, maximized over time, retaining its dependence on gap height:

$$\max_t \ \tau_{xy}(y,t) = \max_t Im\left(-\delta V_0 \eta^* e^{i\omega t}\frac{\cosh(\delta(H-y))}{\sinh(\delta H)}\right). \tag{20}$$

For any fixed gap height, the maximum stress response reduces to analysis of this function as a function of the material and experimental parameters. At the lower plate, the shear stress response function is easily derived (by finding the time of maximum stress over each period $2\pi/\omega$ and then evaluating at that time):

$$\tau_{xy}^{\max}(\rho, \lambda_0, \eta_0, \omega, H) = V_0|\delta||\eta^*||\coth(\delta H)|. \tag{21}$$

4.2. Height-dependent oscillatory structure in shear stress signals

The simplest dependence of $\tau_{xy}^{\max}(\rho, \lambda_0, \eta_0, \omega, H)$, Eq. (21), is with respect to H, the layer height, for which the dependence is proportional to $|\coth(\delta H)|$. Thus, the H-dependence reduces to a real-valued function of a complex argument, δH, where δ is the complex quantity defined in Eqs. (16)–(18). For fixed material properties ρ, η_0 and λ_0, and driving frequency ω, the dependence on H reduces to the evaluation of $|\coth(\delta H)|$ along the ray δH in the complex plane. Fig. 1 provides a graph of the complex values of $\coth(\delta H)$ for a range of H in three physically distinct model fluids: a strongly elastic fluid with $\eta_0 = 1000$ g/cm s and $\lambda_0 = 10$ s, a viscoelastic fluid with $\eta_0 = 100$ g/cm s and $\lambda_0 = 1$ s, and a nearly viscous fluid with $\eta_0 = 1$ g/cm s and $\lambda_0 = .01$ s. The spiral nature of the $\coth(\delta H)$ function simply reflects the exponential behavior for real δ and the oscillatory behavior for imaginary δ. Clearly the polar angle of the complex number δ (i.e. the ray δH) determines whether the stress signals are dominated by exponential or oscillatory behavior of the coth function. This is made precise just below.

Fig. 2 plots the transfer function $\tau_{xy}^{\max}(\rho, \lambda_0, \eta_0, \omega, H)$, which is proportional to the modulus of the complex-valued spiral in Fig. 1, for the same three model fluids. Clearly, there are oscillations versus layer height in the shear stress signal at the driven plate (in the highly elastic and viscoelastic regimes), with envelopes of the successive peaks and valleys that derive from the exact formula. The peaks and valleys of Fig. 2 correspond to the apogee and perigee of Fig. 1, respectively.

The apparent regularity of the locations of the peaks and valleys in the maximum plate stress signal versus H is dependent on the fluid parameters and frequency chosen in Fig. 1. Note, as we approach the viscous limit, the peaks and valleys vanish. If we express $|\coth(\delta H)|$ as follows,

$$|\coth(\delta H)|^2 = \frac{\sin^2(2\beta H) + \sinh^2(2\alpha H)}{(\cos(2\beta H) - \cosh(2\alpha H))^2}, \tag{22}$$

the dual periodic and exponential dependence is transparent. If the material parameters yield α small with respect to β, for instance a model fluid with $\eta_0 \approx 100$ cm g/s with a relaxation time of approximately 1 s, which renders α smaller than β by an order of

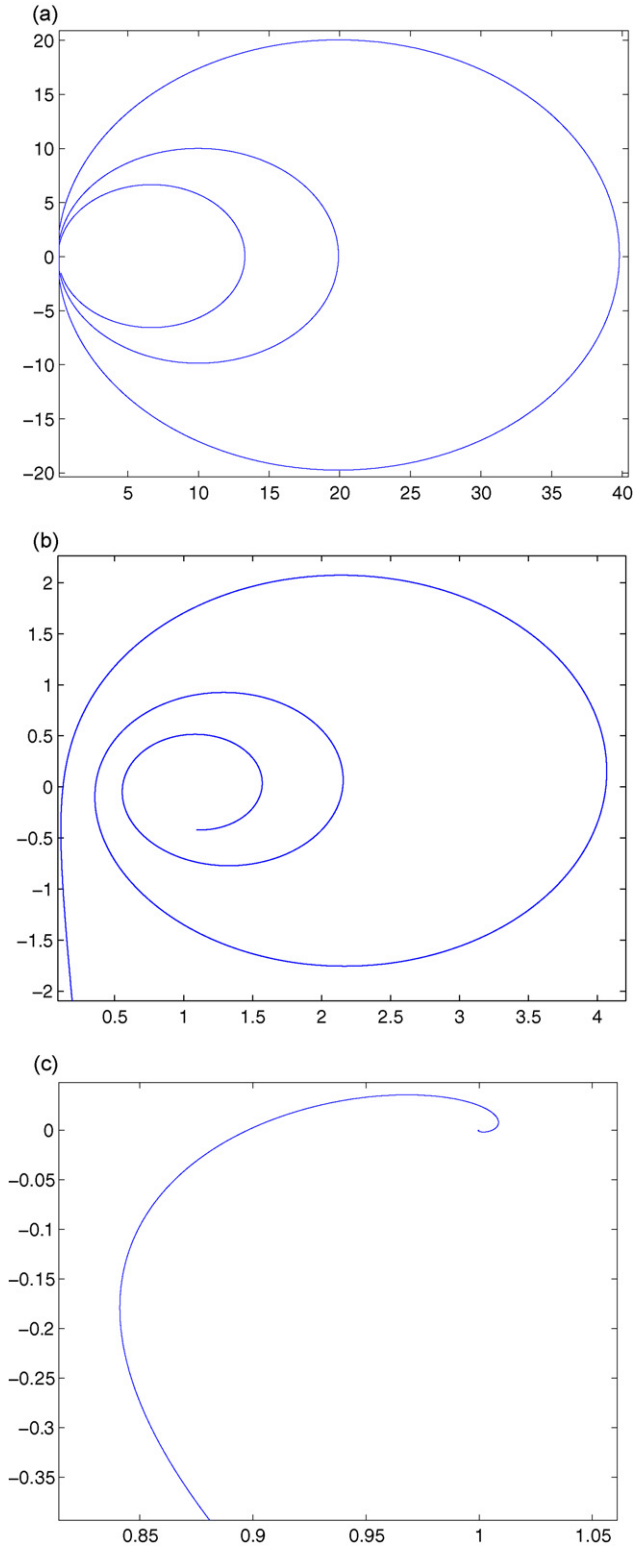

Fig. 1. Evaluation of $\coth(\delta H)$ as a complex-valued function over a range $[H_{\min}, H_{\max}]$ for three model fluids: counter-clockwise from the top, a highly elastic fluid with Maxwell parameters $\eta_0 = 1000$ g/cm s, $\lambda_0 = 10$ s, a viscoelastic fluid with $\eta_0 = 100$ g/cm s, $\lambda_0 = 1$ s, and a fluid near the viscous limit with $\eta_0 = 1$ g/cm s, $\lambda_0 = 0.01$ s. Henceforth, we refer to these parameter choices as Model Fluid 1, 2 and 3. For future reference, we note that $\alpha/\beta = 0.0080$ for Model Fluid 1, $\alpha/\beta = 0.0791$ for Model Fluid 2 and $\alpha/\beta = 0.9391$ for Model Fluid 3.

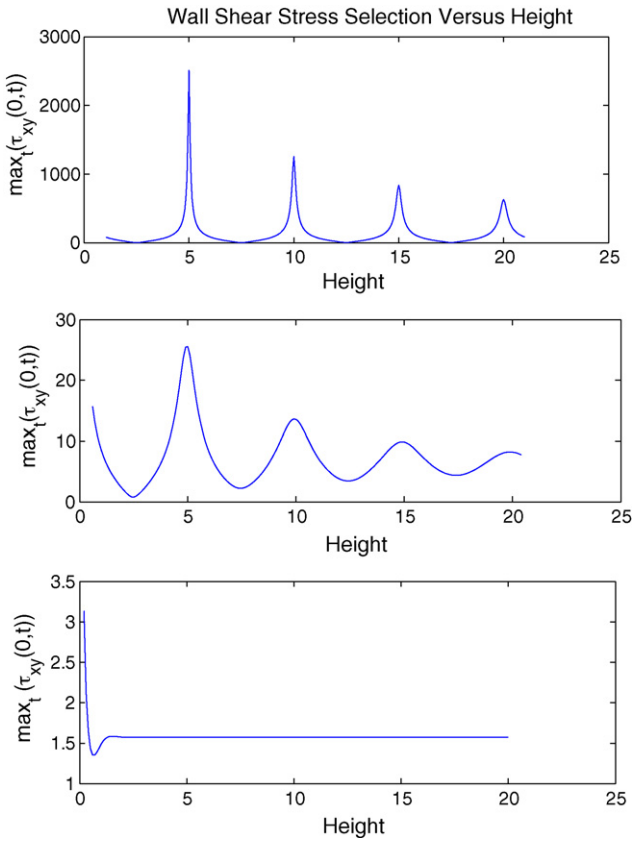

Fig. 2. Maximum shear stress at the lower plate versus layer depth (Eq. (21)) for the three model fluids. The peaks and valleys of the response function correspond to the apogee and perigee, respectively, of the spirals in Fig. 1. For these runs the driving conditions are $A = 0.1$ cm and $\omega = 1$ Hz.

magnitude, then the peaks are very regularly spaced. In a viscous fluid, such as Model Fluid 3 in Figs. 1 and 2, $\alpha = \beta$ and the oscillatory structure vanishes.

From (19), we also have a closed-form expression for the first normal stress difference $N_1 = \tau_{xx}$ (since $\tau_{yy} = 0$). Fig. 3 is a plot of $\tau_{xx}^{\max}$ and $\tau_{xx}^{\min}$ at $y = 0$, again for a range of layer depths. Note that the maxima and minima occur at the same values of H as the maximum shear stress. This property will be illustrated in more depth below.

4.2.1. *Lissajous figures*

Following the work of [6,7], Fig. 4 presents Lissajous figures which show the dynamics of shear stress versus shear rate for a

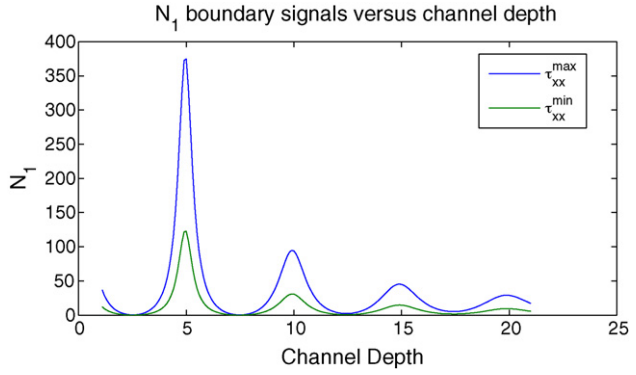

Fig. 3. Maximum and minimum first normal stress difference N_1 at the lower plate versus layer depth (Eq. (21)) for Model Fluid 2 of Figs. 1 and 2 (note $\tau_{yy} = 0$ after transients have passed).

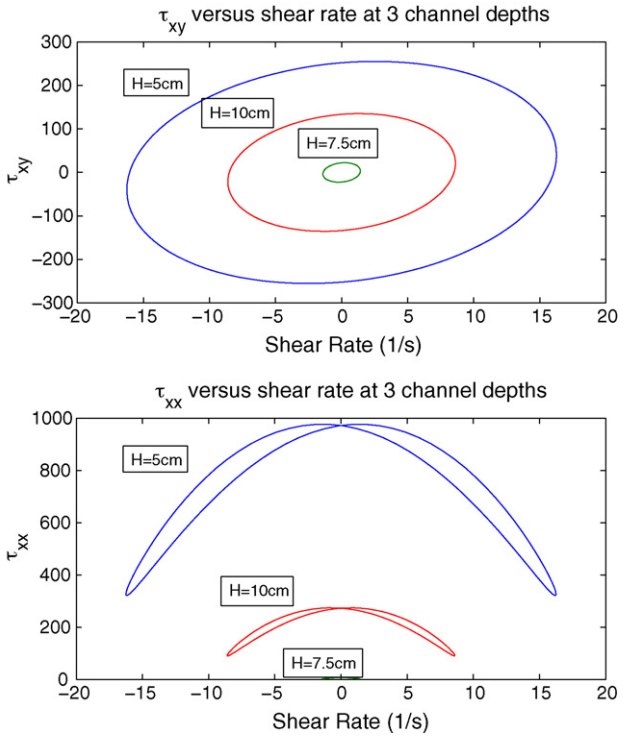

Fig. 4. Lissajous figures of shear and normal stress versus shear rate of Model Fluid 2 for three distinct layer heights, $H = 5, 7.5, 10$ cm, with a driving frequency of 1 Hz and lower plate displacement of 0.1 cm. (a) Shear stress versus shear rate. (b) Normal stress versus shear rate.

given model experiment. For this sweep, we present only the Lissajous figures for Model Fluid 2, but recognize that Model Fluid 1 will exaggerate the results of Fig. 2, while Model Fluid 3 suppresses the phenomenon entirely. For linear viscoelastic fluids in a semi-infinite domain, the Lissajous figure is a slanted, thin ellipse where the slant angle is determined by the ratio β/α of the real and complex parts of δ [7], and is given as $\phi = \tan^{-1}\alpha/\beta$. In the viscous fluid limit, where $\alpha = \beta$, the slant angle of the ellipse is precisely 45°. Fig. 4, also shows the extreme values of shear stress at these heights for Model Fluid 2 which are 3 of the data points in Fig. 3.

Next, in Fig. 5 we give the analogous Lissajous figures of the normal stress τ_{xx} versus shear rate, for the same simulations of Fig. 4. The key features are: the normal stress has half the period of the shear stress and shear rate, and the extreme values are clearly non-monotone versus layer height H. Lastly, in Fig. 6, we present Lissajous figures of the first normal stress difference N_1 versus the shear stress τ_{xy}. We find non-monotone behavior consistent with

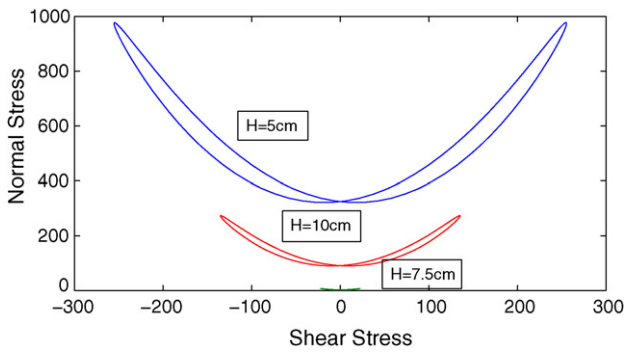

Fig. 5. Time-dependent normal stress versus shear stress loops for Model Fluid 2 for the same data as Fig. 4.

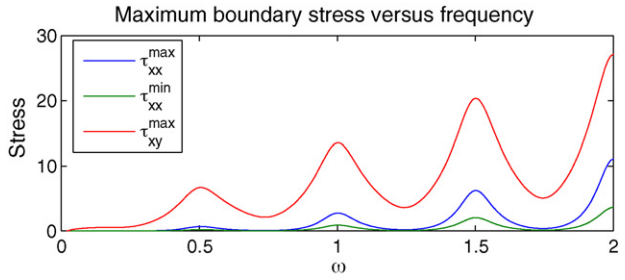

Fig. 6. A frequency sweep of extreme wall shear and normal stresses for Model Fluid 2 over the frequency range [0,2].

previous Figures, but further, oscillations in the relative extreme values of N_1 and τ_{xy}. Thus, changing the height of the layer also controls the relative magnitude of the stress components. It is also clear that the maxima and minima of the shear and normal stresses occur at the same times.

4.3. Frequency sweeps

Next, we turn to the frequency-dependence of the shear and normal stress transfer functions. Their dependence on ω is more complicated than H, yet their behavior again is simply a matter of evaluating the explicit formulas (19) and (21). Fig. 6 shows the result for Model Fluid 2 over the frequency range $0 < \omega < 2$ for $H = 10$ cm. For the previous H sweep in Fig. 2, we fixed $\omega = 1$, and $H = 10$ was near a peak in the shear stress transfer function. From Fig. 6, it is clear that by increasing or decreasing ω from 1, the extreme interfacial stress functions for normal and shear stress walk off of the peak value, but that additional peaks occur near 0.5 cm and 1.5 cm. There is no need to restrict to studying the transfer of interfacial stress as a function of a single variable. Fig. 7 gives the transfer function for extreme interfacial shear stress over several parameters, such as ω and H, with a range of frequency and layer height given by $\omega \in [0,2]$ and $H \in (0,10]$ for Model Fluid 2. From graphs such as Fig. 7, one can find local maxima and minima of the transfer functions over ranges of the driving and fluid parameters.

4.4. Scaling behavior for wall extreme values of shear and normal stress

Before proceeding to the dependence on the UCM material parameters η_0, λ_0 and ρ, we pause to examine the scaling behavior of the oscillatory structure versus H and ω. Namely, the *regularity* of the peaks and valleys versus H and ω is quite striking. From the analysis versus H, it is clear that the behavior is not periodic, except

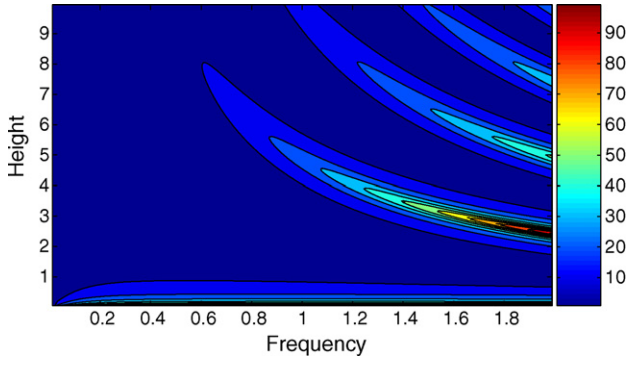

Fig. 7. A parameter sweep of extreme wall shear stress for Model Fluid 2 over the range of parameters $\omega \in [0,2]$ Hz and $H \in (0,10]$ cm.

in the elastic limit of $\alpha \ll \beta$. The elastic solid limit is reached by letting η_0 and λ_0 become large while maintaining a constant ratio. The attenuation and wave length parameters (α and β) become:

$$\lim_{\substack{\eta_0 \to \infty \\ \lambda_0 \to \infty \\ \eta_0/\lambda_0 = c}} \alpha = 0 \tag{23}$$

$$\lim_{\substack{\eta_0 \to \infty \\ \lambda_0 \to \infty \\ \eta_0/\lambda_0 = c}} \beta = \omega\sqrt{\frac{\rho\lambda_0}{\eta_0}}, \tag{24}$$

and the extreme shear stress transfer function, Eq. (21), becomes,

$$\tau_{xy}^{max} = V_0\beta\eta''|\cot\ \beta H|. \tag{25}$$

Thus, the extreme shear stress transfer function, in the elastic limit, exhibits asymptotes at,

$$\beta = \frac{\pi}{H}k \quad k \in \{0, 1, 2, \ldots\} \tag{26}$$

If we now identify the elastic wave speed,

$$c_0 = \sqrt{\frac{\eta_0}{\lambda_0\rho}}, \tag{27}$$

then β is given by,

$$\beta = \frac{\omega}{c_0}, \tag{28}$$

and thus the resonance condition can be restated in the elastic limit as:

$$\frac{c_0}{2\bar{\omega}H}k = 1 \quad k \in \{0, 1, 2, \ldots\}, \tag{29}$$

where $\omega = 2\pi\bar{\omega}$. In terms of the frequency sweep, the fundamental frequency, denoted $\bar{\omega}_{\text{fund}}$, becomes

$$\bar{\omega}_{\text{fund}}^{\text{peak}} = \frac{c_0}{2H}, \tag{30}$$

which is equivalent to a period of plate oscillation that matches the round trip travel time of the elastic shear wave. Additional resonance frequencies are integer multiples of this fundamental frequency. Expressing Eq. (29) with respect to any of the fluid or control parameters gives a resonance condition for that value. For example,

$$H_{\text{peak}}^{\text{fund}} = \frac{c_0}{2\bar{\omega}}. \tag{31}$$

To extend these results from the elastic solid limit to any viscoelastic fluid, consider the non-dimensional parameter α/β. Since $\alpha < \beta$, then for any viscoelastic fluid $\alpha/\beta \in (0,1)$. As we have seen in Eqs. (23) and (24), the elastic solid limit corresponds to $\alpha/\beta = 0$, and further in the viscous limit $\lambda_0 \to 0$ it is clear that $\alpha/\beta = 1$. With respect to this parameter α/β, a measure of where a fluid is in the elastic solid to viscous limit, one could gauge the efficacy of using the elastic solid resonance condition as an estimate for the peaks and valleys of the transfer functions. Table 1 explores the usage of (31) as an estimate for the peaks and valleys of the extreme shear stress for a wide range of α/β, and confirms that as $\alpha/\beta \to 1$, the usage of (31) as a prediction of the first fundamental peak of the transfer function becomes dramatically worse.

Fig. 8 gives another interpretation of the data in Table 1, by graphing the percentage error as a function of α/β in the loglog scale. The data points are fit here by a power law, which becomes a line in the loglog scale, and exhibits the nature of the walk off from pure resonance behavior as a fluid deviates from the elastic limit.

Table 1
As the fluid parameters are varied from the nearly elastic to the nearly viscous regime, the occurrence of the first fundamental in H walks off from the elastic resonance limit exponentially

α/β	$H_{\text{fund}}^{\text{approx}}$	$H_{\text{fund}}^{\text{exact}}$	% error
0.000796	0.5	0.49999	<0.00001
0.007957	0.5	0.4999	<0.00001
0.015913	0.5	0.4998	0.0400
0.026515	0.5	0.4995	0.1001
0.039726	0.5	0.4989	0.2205
0.079075	0.5	0.4955	0.9082
0.172598	5	4.819	3.756
0.237477	5	4.659	7.319
0.552726	5	3.820	30.89

In summation, for any fluid with known zero shear viscosity η_0 and relaxation time λ_0, one can get an approximation of the fundamental layer height that will maximize stress transfer. The accuracy of this approximation can be gleaned by from Table 1. Further, by solving Eq. (29) for any of the variables, the following approximate scaling conditions (exact in the elastic limit) are identified:

$$\bar{\omega}_{\text{peak}}^{k} \approx \frac{kc_0}{2H} \tag{32}$$

$$H_{\text{peak}}^{k} \approx \frac{kc_0}{(2\bar{\omega})} \tag{33}$$

$$\lambda_{\text{peak}}^{k} \approx k^2 \frac{1}{4H^2\bar{\omega}^2}\frac{\eta_0}{\rho} \tag{34}$$

$$\rho_{\text{peak}}^{k} \approx k^2 \frac{1}{4H^2\bar{\omega}^2}\frac{\eta_0}{\lambda} \tag{35}$$

$$\eta_{\text{peak}}^{k} \approx \frac{4H^2\bar{\omega}^2\lambda\rho}{k^2}. \tag{36}$$

4.5. Transfer function dependence on η_0, λ_0 and ρ

We now illustrate the inferences gained in the previous section. Namely, there is an underlying oscillatory structure in the extreme values of boundary stresses with respect to all parameters in the model. Figs. 9–11 show this behavior for the baseline properties of Model Fluid 2 with respect to variations in the elastic relaxation time λ_0, the zero strain rate viscosity η_0 and the fluid density ρ. Note the stress peaks are quite well approximated by the elastic limit scaling behavior presented above, formulas (34)–(36).

5. Transfer function structure for a Giesekus fluid

Here we refer to [4] for a numerical solution to the analogous problem where the constitutive equation is given by a single mode

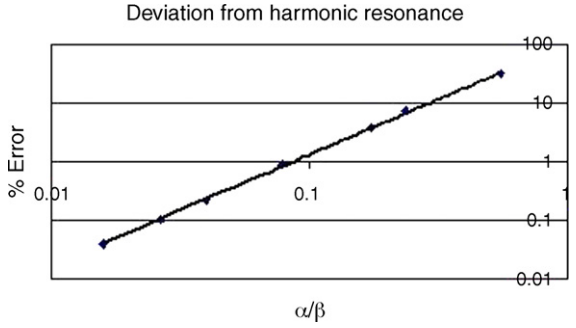

Fig. 8. Percent error calculations for using Eq. (27) to predict peaks of the extreme shear stress for different viscoelastic fluids with given ratios α/β. The scale is loglog and thus the trend-line shown is a simple power law fit to the data.

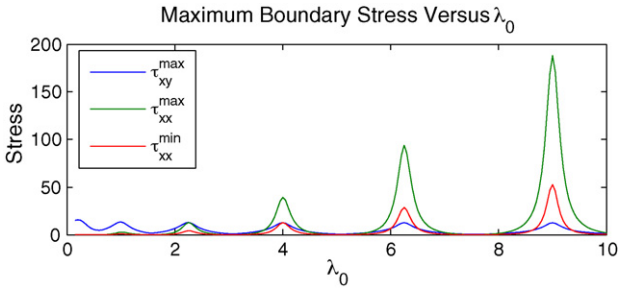

Fig. 9. Relaxation time sweep of extreme boundary shear and normal stresses with respect to λ_0 variations of Model Fluid 2. We fix η_0 and ρ of Model Fluid 2 with boundary values $\omega = 1$ Hz, $A = 0.1$ cm and $H = 10$ cm then perform a relaxation time sweep. The elastic limit scaling prediction of the kth peak is $\lambda_{\text{peak}}^{k} = 0.25\,k^2$.

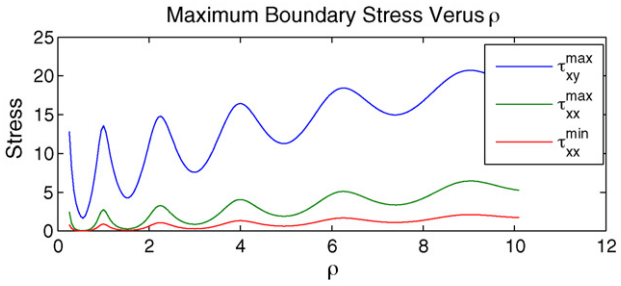

Fig. 10. Density sweep of extreme boundary shear and normal stresses with respect to ρ variations of Model Fluid 2. We fix η_0 and λ_0 of Model Fluid 2 with boundary values $\omega = 1$ Hz, $A = 0.1$ cm and $H = 10$ cm then perform a density sweep. The elastic limit scaling prediction of the kth peak is $\rho_{\text{peak}}^{k} = 0.25\,k^{-2}$.

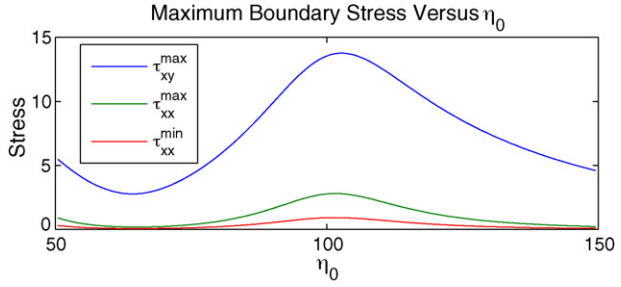

Fig. 11. Zero shear-rate viscosity sweep of extreme boundary shear and normal stresses with respect to η_0 variations of Model Fluid 2. We fix ρ and λ_0 of Model Fluid 2 with boundary values $\omega = 1$ Hz, $A = 0.1$ cm and $H = 10$ cm then perform a zero shear-rate viscosity sweep. The elastic limit scaling prediction of the kth peak is $\eta_{\text{peak}}^{k} = 400\,k^{-2}$.

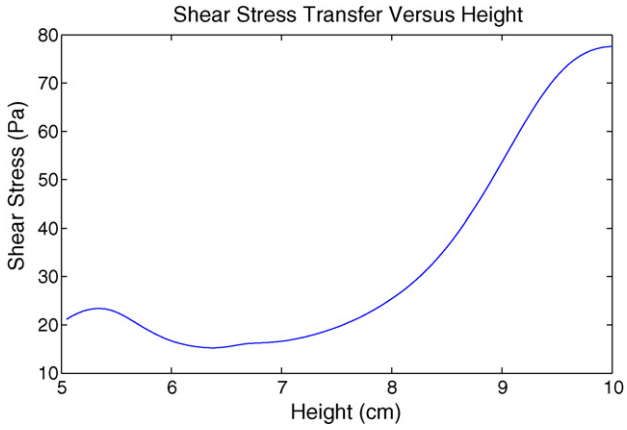

Fig. 12. Maximum shear stress at the lower interface versus channel depth for Model Fluid 2 with a Giesekus mobility parameter of 0.01. The driving conditions here are $\omega = 1$ Hz and $A = 0.1$ cm.

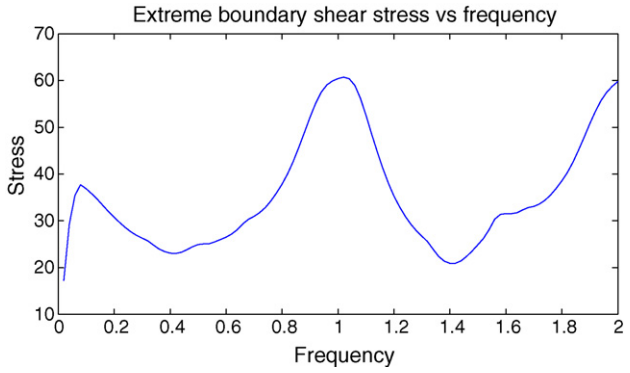

Fig. 13. Maximum shear stress at the lower interface versus frequency for Model Fluid 2 with a Giesekus mobility parameter of 0.01. The driving conditions here are $\omega = 1$ Hz and $A = 0.1$ cm.

Giesekus model. The boundary stress behavior of this paper was, in fact, discovered in this context. Fig. 12 repeats the H sweep of Fig. 2 for Model Fluid 2 parameters together with a mobility parameter value of 0.01. Fig. 13 shows the result of a frequency sweep, while Fig. 14 revisits the Lissajous figures of Section 4.2.1 and obtains the analogous results for this model. The striking feature of Fig. 14 is that non-linearity is evident at $H = 5$ and $H = 10$, but at $H = 7.5$ the fluid exhibits the classic linear behavior (with the elliptical orbit seen in Fig. 4).

The pertinent features of Fig. 11 are that we see a similar height selection mechanism for the transfer of shear stress, and that the figure shows additional non-linear structure. Note that the locations of the maxima and minima are notably different. Fig. 6 contains Lissajous figures for various heights. From the Lissajous figures, it is clear that shear thinning is occurring in the Giesekus fluid at these strains.

6. Stress-controlled versus strain-controlled oscillatory shear

The phenomenon in question has been explored in previous sections for strain-controlled boundary conditions. Alternative boundary conditions, each modeling a different experimental protocol, consist of imposing a periodic stress or strain at either interface. For example, one can impose a periodic shear stress boundary condition at the bottom interface, retaining a stationary top boundary:

$$\tau_{xy}(0, t) = \tau_0 \sin(\omega t), \quad v_x(H, t) = 0. \tag{37}$$

It is straightforward to show that this boundary value problem is equivalent to the strain-controlled problem and solution presented above,

$$v_x(y, t) = Im\left(V_0\ e^{i\omega t}\frac{\sinh\,\delta(H-y)}{\sinh\,\delta H}\right), \tag{38}$$

where V_0 is now complex valued and given by,

$$V_0 = -\frac{\tau_0}{\eta^*\delta}\tanh\,\delta H. \tag{39}$$

To relate the complex number V_0 above to its more natural physical interpretation as the maximum imposed velocity of the lower plate we recast the formula,

$$v_x(y, t) = Im\left(|V_0|e^{i(\omega t+\chi)}\frac{\sinh\,\delta(H-y)}{\sinh\,\delta H}\right), \tag{40}$$

where $\chi = \arg(V_0)$, demonstrating a clear equivalence of the two stress and strain controlled boundary value problems.

Perhaps more physically interesting (especially for applications to lung biology), is a stress free boundary condition at the upper interface together with an oscillatory strain at the lower interface:

$$v_x(0, t) = V_0 \sin(\omega t), \quad \tau_{xy}(H, t) = 0. \tag{41}$$

The solution is a sum of two solutions of (7)–(11),

$$v_x(y, t) = Im\left[e^{i\omega t}\left(V_0\frac{\sinh\,\delta(H-y)}{\sinh\,\delta H} - V_H\frac{\sinh\,\delta(y)}{\sinh\,\delta H}\right)\right], \tag{42}$$

where the stress free condition at the upper interface determines V_H,

$$V_H = V_0 \quad \mathrm{sech}(\delta H). \tag{43}$$

Using a similar approach, one can determine solutions for all four sets of well-posed boundary conditions. Clearly the phenomenon we have identified persists, since it rests on the behavior of hyperbolic functions along rays in the complex plane.

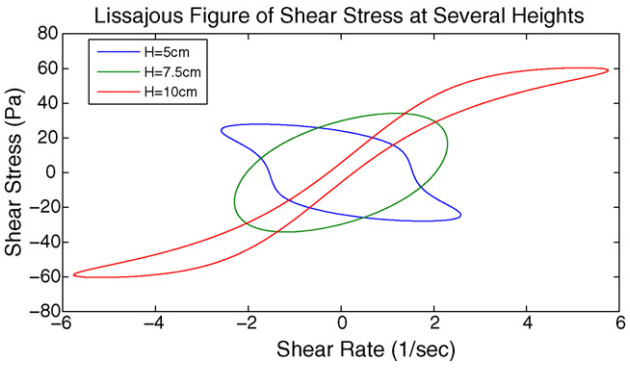

Fig. 14. Shear stress versus shear rate loop for a Giesekus fluid at several heights.

7. Conclusion

The response of a viscoelastic layer in oscillatory shear has been explored with a focus on the extreme values of boundary stress signals. The phenomenon we have identified is an oscillatory structure (non-monotone with many peaks and valleys) in boundary stress signals with respect to all parameters (layer thickness, frequency of imposed shear, or material properties). This structure indicates a redundant mechanism with which to either communicate stress signals, by tuning to the peaks of the structure, or to filter stress by tuning to the valleys. Using the upper convected Maxwell model, we provide a rigorous explanation of the phenomenon, and then illustrate its persistence with a Giesekus model simulation where the results were first discovered. The relevance of these results to the biological setting of pulmonary mucus layers remains for future studies. The implication we have in mind is the ability of epithelial cells or cilia to mechanically sense and respond to the variability in stress signals shown here.

References

[1] J.D. Ferry, Studies of the mechanical properties of substances of high molecular weight. I. A photoelastic method for study of transverse vibrations in gels, Rev. Sci. Inst. 12 (1941) 79–82.
[2] J.D. Ferry, Behavior of concentrated polymer solutions under periodic stresses, J. Polym. Sci. 2 (1947) 593–611.
[3] J.D. Ferry, F.T. Adler, W.M. Sawyer, Propagation of transverse waves in viscoelastic media, J. Appl. Phys. 20 (1949) 1036–1041.
[4] S.M. Mitran, M.G. Forest, L. Yao, B. Lindley, D. Hill, Extenstions of the Ferry shear wave model for active linear and nonlinear microrheology, J. Non-Newtonian Fluid Mech. 154 (2008) 120–135.
[5] D.B. Hill, B. Lindley, M.G. Forest, S.M. Mitran, R. Superfine, Experimental and modeling protocols from a micro-parallel plate rheometer, UNC Preprint, 2008.

[6] R. Keunings, K. Atalik, On the occurrence of even harmonics in the shear stress response of viscoelastic fluids in large amplitude oscillatory shear, J. Non-Newtonian Fluid Mech. 122 (2004) 107–116.
[7] R.S. Jeyaseelan, A.J. Giacomin, Network theory for polymer solutions in large amplitude oscillatory shear, J. Non-Newtonian Fluid Mech. 148 (2007) 24–32.
[8] R.H. Ewoldt, A.E. Hosoi, G.H. McKinley, Rheology of mucin films for Molluscan adhesive locomotion, Abstr. Pap. Am. Chem. Soc. 231 (2006), 387-PMSE.
[9] R.H. Ewoldt, A.E. Hosoi, G.H. McKinley, Rheological fingerprinting of complex fluids using large amplitude oscillatory shear (LAOS) flows, in: Annual Transactions of the Nordic Society of Rheology, Nordic Rheology Conference, Stavanger, Norway, 13–15 June, 2007, pp. 3–8.
[10] R.H. Ewoldt, C. Clasen, A.E. Hosoi, G.H. McKinley, Rheological fingerprinting of gastropod pedal mucus and synthetic complex fluids for biomimicking adhesive locomotion, Soft Matter 3 (5) (2007) 634–643.
[11] L. Preziosi, On an invariance property of the solution to stokes first problem for viscoelastic fluids, J. Non-Newtonian Fluid Mech. 33 (2) (1989) 225–228.
[12] L. Preziosi, D.D. Joseph, Stokes' first problem for viscoelastic fluids, J. Non-Newtonian Fluid Mech. 25 (3) (1987) 239–259.
[13] R. Tarran, B. Button, M. Picher, A.M. Paradiso, C.M. Ribeiro, E.R. Lazarowski, L. Zhang, P.L. Collins, R.J. Pickles, J.J. Fredberg, R.C. Boucher, Normal and cystic fibrosis airway surface liquid homeostasis: the effects of phasic shear stress and viral infections, J. Biol. Chem. 280 (42) (2005) 35751–35759.
[14] R.G. Larson, Constitutive Equations for Polymer Melts and Solutions, Butterworths, Guilford, UK, 1988.
[15] R. Bird, C. Curtis, R. Armstrong, O. Hassenger, Dynamics of Polymer Fluids, vol. 1 & 2, Wiley, New York, 1987.
[16] J.M. Dealy, Misuse of the term pressure in rheology, Rheol. Bull. 77 (2008) 11–13.
[17] T.T. Tee, J.M. Dealy, Nonlinear viscoelasticity of polymer melts, Trans. Soc. Rheol. 19 (1975) 595–615.